Engineering Geology 359 (2025) 108443

Contents lists available at ScienceDirect

Engineering Geology

journal homepage: www.elsevier.com/locate/enggeo

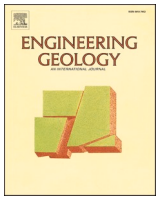

Insights into the dimensionless stability analysis of homogeneous slopes

Domenico Gallipoli *, Leonardo Maria Lalicata

Dipartimento di Ingegneria Civile, Chimica e Ambientale, Università di Genova, Italy

ARTICLE INFO

Keywords:
Slope stability
Non-dimensional analysis
Slip surface geometry
Design charts
Closed-form solutions

ABSTRACT

The paper explores the relationship between the normalised safety factor and the non-dimensional material parameter of homogeneous slopes. It introduces a novel non-dimensional slip geometry parametrisation within Bishop limit equilibrium solution, which is defined by the entry tangent, entry point and exit point. These parameters are directly linked to the physical viability of the slip surface and can therefore be mathematically constrained to account for all and only admissible failure mechanisms. The relationship between the normalised safety factor and the non-dimensional material parameter is decomposed into linear and non-linear components, which respectively describe the contributions of cohesion and friction to slope stability. These components vanish as the material parameter approaches zero and infinity, respectively, thus recovering the two limit cases of purely frictional and purely cohesive slopes. The relationship is interpolated by a closed-form equation, allowing the direct calculation of the factor of safety for virtually any cohesive-frictional slope, including vertical cuts, without requiring further analysis. Non-dimensional charts are derived to readily identify the critical slip surface based on the novel parameter triplet. The transition between shallow and deep failures is marked by a threshold value of the non-dimensional material parameter, which increases for steeper slopes.

1. Introduction

Since the early works of Taylor (1937), Bell (1966) and Hoek and Bray (1974), dimensionless charts have been developed to assess the stability of homogeneous cohesive-frictional soil and rock slopes via limit equilibrium methods or upper bound analyses (e.g. O'Connor and Mitchell, 1977; Chandler and Peiris, 1989; Baker et al., 2006; Barnes, 1991; Leshchinsky and San, 1994; Michalowski, 2002; Steward et al., 2011; Sun and Zhao, 2013; Vo and Russell, 2017; Li et al., 2021; Cui et al., 2022; Huang and Ji, 2022; Huang, 2023; Sampa and Schorr, 2024; Park, 2025). More recently, Carranza-Torres and Hormazabal (2018) and Carranza-Torres (2021) revisited the well-known dimensionless diagrams by Hoek and Bray (1974) and recast the information in a form that is more appealing to practitioners involved in the analysis of open pit mine slopes.

Some of these earlier studies have proposed dimensionless relationships between the normalised factor of safety $FoS/\tan\varphi$ and the material parameter $c/(\gamma\, h\tan\varphi)$ (e.g. Michalowski, 2002; Huang, 2023), where FoS, φ, c and γ are the factor of safety, friction angle, cohesion and unit weight, respectively, while h is the slope height. Other works have instead related the normalised factor of safety $FoS/\tan\varphi$ to the inverse of the material parameter $(\gamma\, h\tan\varphi)/c$ (e.g. Carranza-Torres and Hormazabal, 2018; Carranza-Torres, 2021). Finally, other researchers have proposed relationships between three different normalised parameters, namely $\tan\varphi/FoS$, $c/(\gamma\, h\, FoS)$ and $c/(\gamma\, h\tan\varphi)$ (e.g. Hoek and Bray, 1974; Wyllie and Mah, 2004; Read and Stacey, 2009; Steward et al., 2011). The first two approaches, which are formulated in terms of only two non-dimensional parameters, offer the advantage of enabling a direct evaluation of the factor of safety without the need for graphical iterations.

This study provides further insights into the dimensionless stability analysis of homogeneous slopes. Building on the pioneering work of Bell (1966), the study recasts the dimensionless form of Bishop (1955) limit equilibrium equation in terms of a single slice parameter, i.e. the normalised slice abscissa. The proposed formulation simplifies the dimensionless slice summation, particularly when used in conjunction with the newly proposed slip circle parametrisation. This parameterisation incorporates the angle of the slip circle at the entry point, instead of the radius, along with the normalised abscissae of the entry and exit points. As demonstrated by Lalicata et al. (2024), the use of the entry angle instead of the radius offers two key advantages. It ensures that the critical slip circle is included within the search space, improving accuracy, and it excludes unviable slip mechanisms, enhancing computational efficiency by eliminating unnecessary analyses. For instance, low

* Corresponding author at: Dipartimento di Ingegneria Civile, Chimica e Ambientale, Via Montallegro, 1, Università di Genova, 16145 Genova, Italy.
E-mail address: domenico.gallipoli@unige.it (D. Gallipoli).

https://doi.org/10.1016/j.enggeo.2025.108443
Received 8 April 2025; Received in revised form 23 October 2025; Accepted 29 October 2025
Available online 1 November 2025

curvature slip circles with radii approaching infinity, as in very steep slopes, are not captured by standard parametrisations using the radius, but are naturally handled by the proposed alternative. Because the new parameter triplet is intrinsically linked to the physical viability of the slip circle, it can be rigorously constrained to represent all and only admissible failure mechanisms.

This study interpolates the calculated values of the normalised factor of safety $FoS/\tan\varphi$ for various slope inclinations β and material parameters $c/(\gamma\, h\tan\varphi)$ to obtain a closed-form expression that separately accounts for the contributions of cohesive and frictional strength. The normalised factor of safety $FoS/\tan\varphi$ is here related to the material parameter $c/(\gamma\, h\tan\varphi)$, rather than its inverse $(\gamma\, h\tan\varphi)/c$, as in previous works, because this facilitates the description of the limit cases of purely frictional and purely cohesive slopes. The interpolation reveals a threshold value of the slope inclination that marks a transition in frictional behaviour, consistent with similar observations for cohesive behaviour (Taylor, 1937; Steward et al., 2011).

Baker (2003), Steward et al. (2011), Carranza-Torres and Hormazabal (2018) and Carranza-Torres (2021) have also developed dimensionless tools for quickly assessing the geometry of the critical failure mechanism. Steward et al. (2011) provided a qualitative analysis of the failure geometry, while Baker (2003) defined the slip mechanism using complex functions that may be cumbersome for routine applications. Carranza-Torres and Hormazabal (2018) and Carranza-Torres (2021) provided an Excel spreadsheet to compute the dimensionless coordinates of the critical slip surface for shallow to nearly vertical slopes. Building upon these earlier works, this study presents dimensionless charts to define the critical slip surface in terms of the newly proposed parameter triplet for a full range of slopes from shallow to fully vertical.

Simplicity, accuracy and widespread adoption among engineering practitioners justify the use of Bishop (1955) limit equilibrium method in this study. Utili and Crosta (2015) provided a comprehensive review of limit equilibrium methods, among which Bishop (1955) method stands out as the most widely used in design practice, a status reinforced by its endorsement in the Eurocode 7 (EN 1997–1, 2004; Bond et al., 2013). Bishop (1955) method is currently employed for routine stability analyses, particularly when limited data is available and the assumption of soil homogeneity is acceptable. In such cases, dimensionless stability charts based the method of Bishop (1955) offer a practical framework for the preliminary assessment of slope stability, such as in the design of deep open pit mines or road and rail embankments (Hoek and Bray, 1974; Wyllie and Mah, 2004; Read and Stacey, 2009; Carranza-Torres and Hormazabal, 2018; Carranza-Torres, 2021).

In terms of accuracy, the factor of safety of homogeneous slopes calculated by Bishop (1955) method is nearly identical to that calculated by more precise, yet more complex, limit equilibrium methods like Morgenstern and Price (1965) and Spencer (1967) (Abramson et al., 2002). For circular slip surfaces, there are also no significant differences with more sophisticated design approaches, such as limit analysis or shear strength reduction (Duncan, 1996; Carranza-Torres and Hormazabal, 2018). Bishop (1955) method exhibits limitations in cases involving hydraulic gradients, heterogeneous soils or non-circular slip surfaces, but it remains well-suited for analysing the fundamental cohesive-frictional behaviour of homogeneous and seepage-free slopes, as considered in this study. The present work also assumes the absence of tension cracks and an infinite depth of the firm stratum (i.e. Taylor depth parameter $D = \infty$).

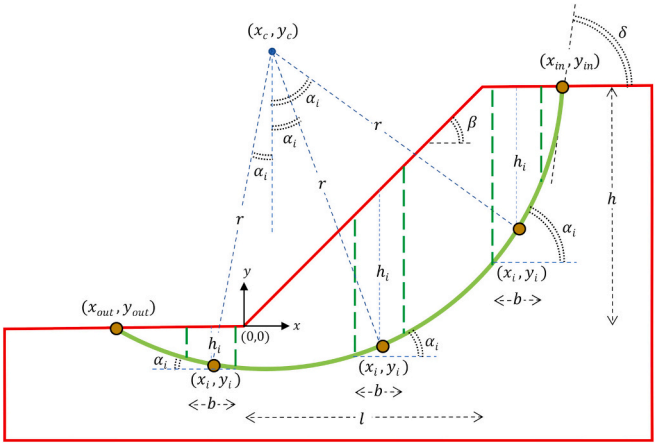

Fig. 1. Parametrisation of circular slip surface in Bishop (1955) method.

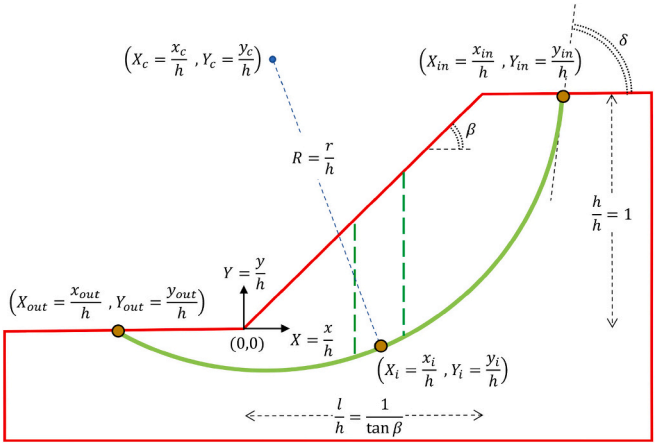

Fig. 2. Dimensionless parametrisation of circular slip surface in Bishop (1955) method.

2. Dimensionless form of Bishop (1955) slope stability equation

The Bishop (1955) method assumes a circular slip surface to impose the vertical and rotational equilibrium of the potentially unstable soil mass. Under this hypothesis, the factor of safety FoS of a homogeneous slope is calculated by discretising the unstable soil mass into n vertical slices, whose interface shear forces are neglected, as:

$$FoS = \frac{1}{\sum_{i=1}^{n}\gamma\, h_i \sin\alpha_i}\sum_{i=1}^{n}\frac{c + \gamma\, h_i \tan\varphi}{\cos\alpha_i + \sin\alpha_i \frac{\tan\varphi}{FoS}} \tag{1}$$

where c, φ and γ are, respectively, the soil cohesion, friction angle and specific weight while h_i and α_i are, respectively, the height and base angle of the generic *ith* slice (Fig. 1). The factor of safety FoS appears on both sides of Eq. (1) and must therefore be iteratively calculated.

Following the work of Bell (1966), Eq. (1) is recast in a dimensionless form relating the normalised factor of safety $F = \frac{FoS}{\tan\varphi}$ to both the non-dimensional material parameter $M = \frac{c}{\gamma\, h\tan\varphi}$ and the slope inclination β as:

$$F = \frac{R^2}{\sum_{i=1}^{n}\left(\sqrt{R^2 - (X_i - X_c)^2} - Y_c + K_i\right)(X_i - X_c)}\sum_{i=1}^{n}\frac{M + \left(\sqrt{R^2 - (X_i - X_c)^2} - Y_c + K_i\right)}{\sqrt{R^2 - (X_i - X_c)^2} + \frac{X_i - X_c}{F}} \tag{2}$$

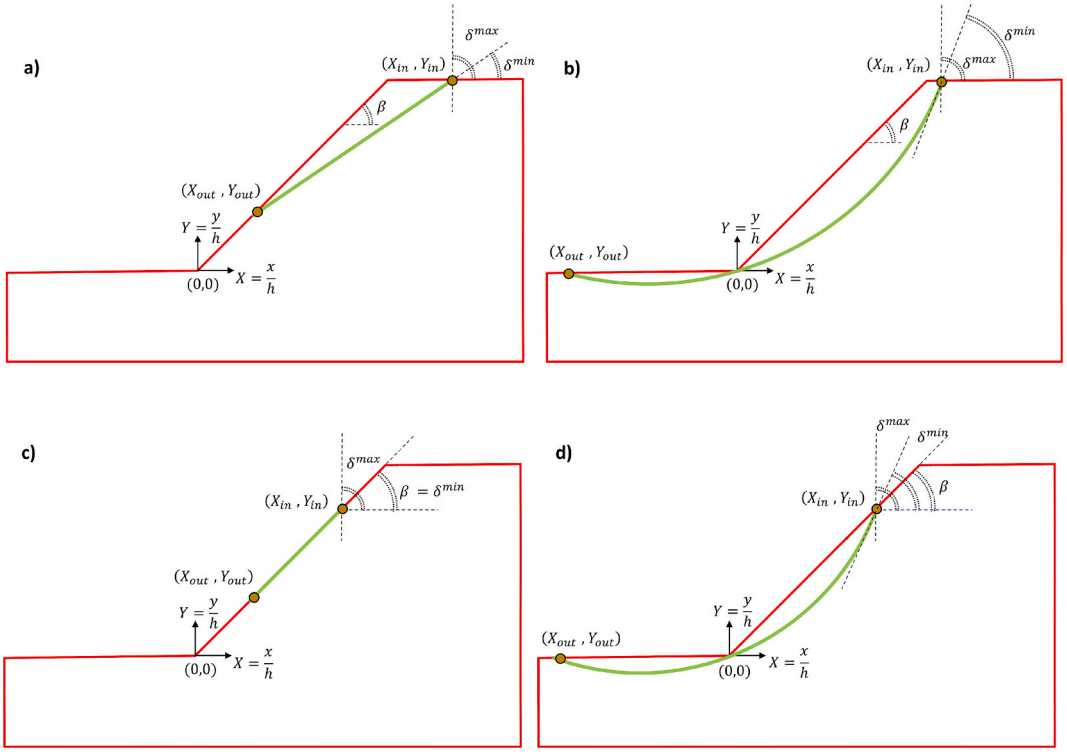

Fig. 3. Possible combinations of entry and exit points: a) entry point on the upper ground and exit point on the scarp, b) entry point on the upper ground and exit point on the lower ground, c) entry and exit points both on the scarp and d) entry point on the scarp and exit point on the lower ground.

with

$$\begin{cases} K_i = 0 & \text{if} \quad X_i \le 0 \\ K_i = X_i \tan\beta & \text{if} \quad 0 \le X_i \le \dfrac{1}{\tan\beta} \\ K_i = 1 & \text{if} \quad X_i \ge \dfrac{1}{\tan\beta} \end{cases}$$

where the meaning of the dimensionless geometric variables is illustrated in Fig. 2. Note that the proposed non-dimensional form of Bishop (1955) solution in Eq. (2) uses a single summation parameter, i.e. the normalised slice abscissa X_i, whereas Bell (1966) employs two distinct summation parameters, i.e. the normalised slice height and the base inclination. Therefore, together with the newly proposed slip circle parameterisation, Eq. (2) streamlines slice summation in computational implementations, as discussed later in the manuscript. The derivation of Eq. (2) is reported in Appendix A.

3. Physically based non-dimensional slip parameters

Limit equilibrium methods search for the critical slip surface with the lowest factor of safety among multiple alternatives. The search domain must therefore be accurately defined to include the critical slip surface and, therefore, to ensure the correctness of the solution. In Bishop (1955) method, slip surfaces are arcs of a circle, typically defined by the radius r along with the two centre coordinates x_c and y_c. While these three parameters are geometrically intuitive, they are not directly linked to the physical viability of the corresponding slip surface, which leads to two limitations. The first limitation is the potential inaccuracy of results due to the exclusion of the critical failure mechanism from the search space, which could result in an overestimation of the factor of safety. The second limitation relates to computational efficiency, as the search space may include parameter triplets corresponding to physically unviable slip circles, leading to unnecessary analyses and a waste of computational resources.

To account for all and only viable failure mechanisms, this work adopts an alternative physically based parameter triplet, consisting of the tangent angle, δ at the entry point of the slip circle, along with the two abscissae of the entry and exit points, x_{in} and x_{out} (Fig. 1). The abscissae x_{in} and x_{out} have already been used to define slip circles but have been associated to the radius r as the third parameter, leading to the same limitations as above. These limitations are here overcome by replacing the radius r with the tangent angle at the entry point, δ, whose value can be mathematically constrained to encompass all and only viable failure mechanisms. The advantage of the proposed parametrisation becomes particularly evident when analysing vertical and nearly vertical slopes, where the critical slip circle veers towards a straight line, as shown later. In such cases, the conventional parametrisation struggles to capture the critical failure mechanism, which tends to a circle of infinite radius.

The following sections employ a non-dimensional form of the newly proposed parameter triplet, consisting of the angle, δ (already dimensionless) plus the two abscissae of the entry and exit points normalised by the slope height, i.e. $X_{in} = \frac{x_{in}}{h}$ and $X_{out} = \frac{x_{out}}{h}$ (Fig. 2). The corresponding ordinates, $Y_{in} = \frac{y_{in}}{h}$ and $Y_{out} = \frac{y_{out}}{h}$ are calculated from the abscissae once the slope geometry is accounted for.

3.1. Upper and lower bounds of parameter δ

The angle, δ at the entry point of the slip circle (Fig. 2) is mathematically constrained by upper and lower bounds, i.e. $\delta^{min} \le \delta \le \delta^{max}$, to ensure the viability of failure mechanisms. The upper bound coincides with the right angle, i.e. $\delta^{max} = \frac{\pi}{2}$, as any value bigger than that would produce a physically meaningless shear surface, while the lower bound δ^{min} is not univocally defined but it depends on the entry and exit points of the slip circle, i.e. on the chosen values of X_{in} and X_{out}. To calculate δ^{min}, four cases corresponding to different combinations of entry and exit points are considered, thus covering all geometrically possible slip

mechanisms in Fig. 3.

3.1.1. Case a)

For the case of entry point on the upper ground, i.e. $X_{in} \geq \frac{1}{\tan\beta}$, and exit point on the scarp, i.e. $0 < X_{out} < \frac{1}{\tan\beta}$, the lower bound, δ^{min} corresponds to a slip circle of infinite radius degenerating into a straight line (Fig. 3a) and is therefore calculated as:

$$\delta^{min} = \arctan\frac{Y_{in} - Y_{out}}{X_{in} - X_{out}} \tag{3}$$

This value of δ^{min} is a lower bound because any smaller value would produce a physically inadmissible circle with negative curvature, i.e. with a concavity towards the ground. As $Y_{in} = 1$ and $Y_{out} = X_{out}\tan\beta$ (see Fig. 3a), the angle δ^{min} of Eq. (3) is recast in terms of the slope inclination β and the non-dimensional abscissae X_{in} and X_{out} as:

$$\delta^{min} = \arctan\left(\frac{1 - X_{out}\tan\beta}{X_{in} - X_{out}}\right) \tag{4}$$

3.1.2. Case b)

For the case of entry point on the upper ground, i.e. $X_{in} \geq \frac{1}{\tan\beta}$, and exit point on the lower ground, i.e. $X_{out} < 0$, the lower bound, δ^{min} corresponds to a slip circle passing through the slope toe, i.e. through the origin of the reference system (Fig. 3b), and is therefore calculated according to Appendix B as:

$$\delta^{min} = \arctan\frac{2X_{in} - X_{out}}{X_{in}^{\,2} - X_{in}X_{out} - 1} \tag{5}$$

Note that, in this case, δ^{min} is a strict lower bound, i.e. $\delta^{min} < \delta$, since any value of δ equal to or smaller than δ^{min} would produce an inadmissible slip circle emerging at the ground surface at an intermediate location. Moreover, for specific pairs of the normalised abscissae X_{in} and X_{out}, the value of $\tan\delta^{min}$ obtained from Eq. (B4) may be negative and, therefore, the lower bound δ^{min} calculated from Eq. (5) may exceed the upper bound $\delta^{max} = \frac{\pi}{2}$, which is of course unrealistic. Whenever this occurs, the corresponding pair X_{in} and X_{out} does not correspond to any valid slip circle and must be excluded from the search space.

3.1.3. Case c)

For the case of entry and exit points both on the scarp, i.e. $0 < X_{in} < \frac{1}{\tan\beta}$ and $0 < X_{out} < \frac{1}{\tan\beta}$, the lower bound δ^{min} corresponds to a slip circle of infinite radius degenerating into a straight line on the slope surface (Fig. 3c) and is therefore calculated as:

$$\delta^{min} = \beta \tag{6}$$

This value of δ^{min} is a lower bound because any smaller value would produce a physically inadmissible circle with negative curvature, i.e. with a concavity towards the ground.

3.1.4. Case d)

For the case of entry point on the scarp, i.e. $0 < X_{in} < \frac{1}{\tan\beta}$, and exit point on the lower ground, i.e. $X_{out} < 0$, the lower bound δ^{min} corresponds, as in case b), to a slip circle passing through the slope toe (Fig. 3d) and is therefore calculated according to Appendix B as:

$$\delta^{min} = \arctan\frac{(2X_{in} - X_{out})\tan\beta}{X_{in}(1 - \tan^2\beta) - X_{out}} \tag{7}$$

As in case b), δ^{min} represents a strict lower bound, i.e. $\delta^{min} < \delta$, because any value of δ equal to or smaller than δ^{min} would yield an inadmissible slip circle emerging at the ground surface at an intermediate location. Moreover, if Eq. (7) calculates $\delta^{min} > \delta^{max} = \frac{\pi}{2}$ (i.e. if $\tan\delta^{min}$ in Eq. (B5) is negative), the corresponding pair X_{in} and X_{out} is physically inadmissible and must be excluded from the search space.

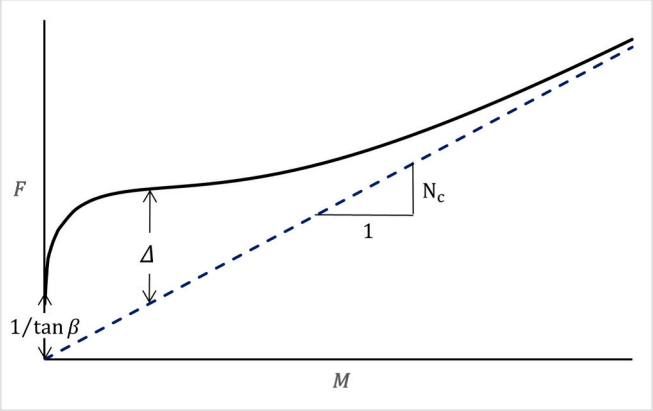

Fig. 4. Schematic relationship between normalised factor of safety F and non-dimensional material parameter M for a generic inclination β.

3.2. Mapping relationships between dimensionless parameter spaces

Eq. (2) calculates the normalised factor of safety F of a slip circle defined by the non-dimensional values of radius R, centre abscissa X_c and centre ordinate Y_c. The same slip circle can be defined by the alternative, physically based non-dimensional parameter triplet consisting of the entry angle δ, entry point abscissa X_{in} and exit point abscissa X_{out}. If this alternative triplet is chosen, Eq. (2) can still be used to calculate the normalised factor of safety F, provided that the following relationships are employed to map between the two dimensionless parameter spaces (see Appendix C for a proof):

$$R = \frac{1}{2}\frac{(X_{in} - X_{out})^2 + (Y_{in} - Y_{out})^2}{\sin\delta(X_{in} - X_{out}) - \cos\delta(Y_{in} - Y_{out})}$$

$$X_c = X_{in} - R\sin\delta$$

$$Y_c = Y_{in} + R\cos\delta \tag{8}$$

Eq. (8) can be tailored to each of the four cases a), b), c) and d) of Section 3.1 by expressing the ordinates Y_{in} and Y_{out} in terms of the corresponding abscissae X_{in} and X_{out} as:

a) $Y_{in} = 1$ and $Y_{out} = X_{out}\tan\beta$;
b) $Y_{in} = 1$ and $Y_{out} = 0$;
c) $Y_{in} = X_{in}\tan\beta$ and $Y_{out} = X_{out}\tan\beta$;
d) $Y_{in} = X_{in}\tan\beta$ and $Y_{out} = 0$.

In Eq. (2), the mid-width abscissa of the i^{th} slice X_i can also be expressed as a function of the entry and exit abscissae X_{in} and X_{out} (Fig. 2) as:

$$X_i = X_{out} + \frac{X_{in} - X_{out}}{n}\left(i - \frac{1}{2}\right) \tag{9}$$

where n is the number of equally wide slices in which the slope has been discretised.

Using Eqs. (8) and (9), the normalised factor of safety F of a slip circle, defined by the dimensionless parameter triplet δ, X_{in} and X_{out}, can be calculated from Eq. (2) as a straightforward summation over the index i, without the need to introduce any slice parameter.

4. Relationship between dimensionless variables F, M and β

Drawing inspiration from the work of Carranza-Torres and Hormazabal (2018), and building upon subsequent related research (Huang and Ji, 2022; Huang, 2023; Sampa and Schorr, 2024), this study proposes a novel physically based relationship linking the normalised factor of safety $F = \frac{FoS}{\tan\varphi}$ to the non-dimensional material parameter $M = \frac{c}{\gamma h\tan\varphi}$

Table 1
Parameters of dimensionless relationship between normalised factor of safety F and material parameter M for different inclinations β.

Inclination β [°]	Asymptotic slope N_c		Parameter A	Parameter B	Parameter C
15	5.52	Eq.	3.594	0.407	2E-08
20	5.52	(12a)	3.345	0.402	2E-08
25	5.52		2.927	0.399	2E-08
30	5.52		2.611	0.398	2E-08
35	5.52		2.336	0.400	2E-08
40	5.52		2.085	0.404	2E-08
45	5.52		1.729	0.413	2E-08
50	5.52		1.417	0.410	2E-08
55	5.45	Eq.	0.088	0.843	1.E-08
60	5.23	(12b)	0.089	0.861	1.E-08
65	5.00		0.087	0.879	1.E-08
70	4.77		0.084	0.892	1.E-08
75	4.54		0.080	0.904	1.E-08
80	4.30		0.074	0.916	1.E-08
85	4.05		0.069	0.927	1.E-08
90	3.83		0.065	0.934	1.E-08

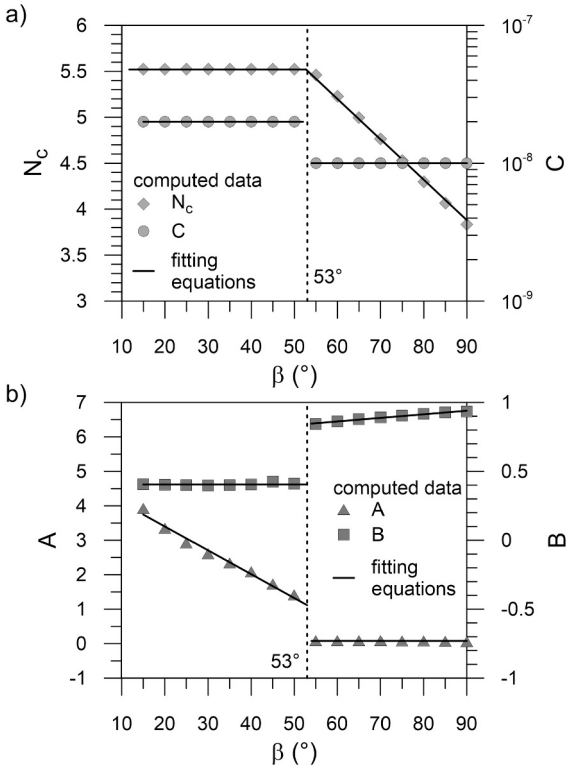

Fig. 5. Interpolation across slope inclinations β of: a) asymptotic slope N_c and fitting parameter C and b) fitting parameters A and B.

for a given slope inclination β. The physical significance of the proposed relationship lies in the explicit separation of the two contributions of cohesive and frictional strength. As schematically shown in Fig. 4 for a generic slope inclination β, the normalised factor of safety F varies with the material parameter M as the sum of a linear term with slope N_c (cohesive contribution) and a non-linear term Δ (frictional contribution) that tends to zero as M approaches infinity:

$$F = N_c M + \Delta \tag{10}$$

The mathematical form of Eq. (10) is dictated by the requirement that, when $M = \frac{c}{\gamma h \tan\varphi} = \infty$ (i.e. for a purely cohesive slope with $c > 0$ and $\varphi = 0$), the frictional contribution Δ must vanish and the normalised factor of safety F must approach a linear asymptote passing through the origin. This is necessary because, only in this case, the calculated factor of safety FoS is independent of the friction angle φ and solely depends on the cohesion c as:

$$F = N_c M \;\Rightarrow\; \frac{FoS}{\tan\varphi} = N_c \frac{c}{\gamma h \tan\varphi} \;\Rightarrow\; FoS = N_c \frac{c}{\gamma h} \tag{11}$$

Note that Eq. (11) indicates that the asymptotic slope $N_c = \frac{FoS\ \gamma\ h}{c}$ coincides with the stability number of Taylor (1937) for cohesive slopes, further corroborating the formulation of Eq. (10).

Eq. (10) also dictates that the cohesive contribution $N_c M$ vanishes when $M = \frac{c}{\gamma\ h \tan\varphi} = 0$ (i.e. for a purely frictional slope with $c = 0$ and $\varphi > 0$). In this case, the normalised factor of safety F coincides with the frictional contribution Δ, which must equal $\frac{1}{\tan\beta}$ to correctly predict the factor of safety of an infinite slope, i.e. $F = \frac{FoS}{\tan\varphi} = \Delta = \frac{1}{\tan\beta} \Rightarrow FoS = \frac{\tan\varphi}{\tan\beta}$ (Taylor, 1948). This is because, for a purely frictional slope, the critical slip mechanism is as shallow as the ground surface, mimicking an infinite slope failure, as indicated by Carranza-Torres and Hormazabal (2018) and Carranza-Torres (2021).

The decomposition of Eq. (10) into cohesive and frictional contributions is therefore rigorously valid at the two extremes of the material parameter range, namely when $M = 0$ and $M = \infty$. In contrast, its extension to intermediate values of the material parameter constitutes a working hypothesis, since in this case the cohesive and frictional components are mathematically inseparable within Bishop solution (Eq. (1)).

Fig. 4 shows that the frictional contribution Δ dominates over the cohesive contribution $N_c M$ when the material parameter $M = \frac{c}{\gamma\ h \tan\varphi}$ is relatively small, which is consistent with the larger weight of the frictional denominator compared to the cohesive numerator. Conversely, the cohesive contribution $N_c M$ prevails over the frictional contribution Δ when the material parameter $M = \frac{c}{\gamma\ h \tan\varphi}$ becomes large, in agreement with the increasing weight of the cohesive numerator relative to the frictional denominator.

Table 1 gives the values of the asymptotic slope N_c for different inclinations β, between 15° and 90°, calculated by analysing the stability of purely cohesive slopes. These values are plotted in Fig. 5a, which shows a discontinuous derivative at an inclination β of about 53° as first observed by Taylor (1937) (see also Steward et al., 2011).

Eq. (10) can be used to directly calculate the factor of safety of a given slope, i.e. without performing any stability analysis, provided that the relationship between the frictional term Δ and the material parameter M is explicitly defined for each inclination. To this end, the frictional term Δ has been here calculated as the difference between the normalised factor of safety F and the linear asymptote $N_c M$ for several pairs of material parameter M, from 0 to 200, and slope inclination β, from 15° to 90°, thus covering virtually all realistic geometrical and material cases. The asymptotic slope N_c has been obtained from Table 1 while the normalised factor of safety F has been evaluated according to Bishop (1955) as the minimum of Eq. (2) across the non-dimensional parametric search space $(X_{in}, X_{out}, \delta)$ using the optimisation algorithm by Lalicata et al. (2024). The normalised factor of safety calculated according to Bishop (1955) is always compared with the corresponding value obtained using Fellenius (1936) and, if the former is smaller, the latter is retained in accordance with Duncan (1996). Fellenius (1936) method is generally less accurate than Bishop (1955) method, tending to underestimate the factor of safety. Nevertheless, there are rare circumstances where it produces a higher factor of safety than Bishop (1955) method. In these cases, Duncan (1996) advises to use Fellenius (1936) instead of Bishop (1955) solution, as the latter may be affected by numerical errors. The results of the present study indicate that this situation occurs for steep slopes, with $\beta > 50°$, when the material parameter M exceeds a threshold value ranging from about 4 to 0.01 as β increases from 50° to 90°, although the difference between the two solutions diminishes progressively for $M > 10$. These results are also consistent with

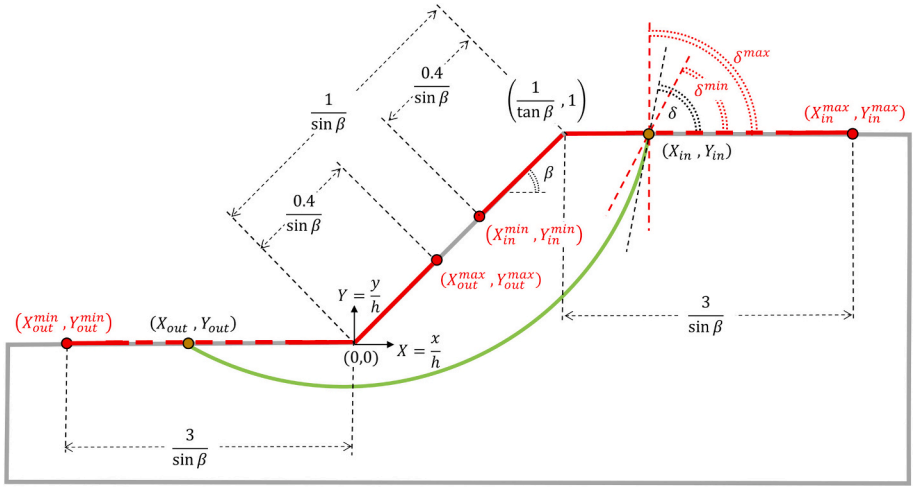

Fig. 6. Bounds of search domain within the normalised parameter space $(X_{in}, X_{out}, \delta)$.

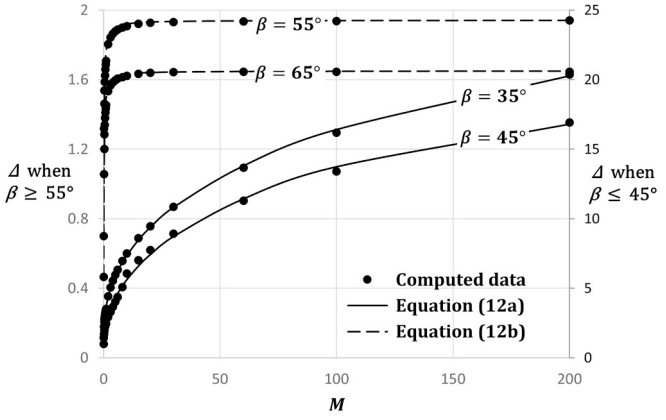

Fig. 7. Variation of frictional term Δ with material parameter M for different inclinations β.

the findings of Michalowski (1995) who showed that, for steep slopes, Bishop (1955) method yields factors of safety lying outside the upper and lower bound solutions.

The search for the minimum value of the normalised factor of safety F takes place inside a bounded parametric space $(X_{in}, X_{out}, \delta)$ to ensure that all and only viable failure mechanisms are considered (Fig. 6):

$$\frac{0.6}{\tan\beta} \le X_{in} \le \frac{1}{\tan\beta} + \frac{3}{\sin\beta}$$

$$-\frac{3}{\sin\beta} \le X_{out} \le \frac{0.4}{\tan\beta}$$

$$\delta^{min} \le \delta \le 90°$$

where $\frac{1}{\sin\beta}$ is the non-dimensional length of the slope face, which coincides with the non-dimensional slope height of 1 for $\beta = 90°$. Recall that the value of δ^{min} is calculated for each pair X_{in} and X_{out} via Eq. (4) or (5) or (6) or (7) depending on which case of Section 3.1 applies.

Fig. 7 plots the relationship between the frictional term Δ, computed as previously described, and the material parameter M for four equally spaced slope inclinations, namely $\beta = 35°$, $\beta = 45°$, $\beta = 55°$ and $\beta = 65°$. The two gentler inclinations exhibit markedly higher frictional contributions and follow distinct trends compared to the two steeper inclinations, indicating a transition occurring within the range $45° < \beta < 55°$. Therefore, similar to the discontinuity in the trend of the cohesive asymptote N_c at $\beta = 53°$ (Fig. 5), the relationship between the frictional contribution Δ and the material parameter M also exhibits a discontinuity over the interval $45° < \beta < 55°$. For modelling purposes, a sharp transition is here assumed at $\beta = 53°$, coinciding with the discontinuity of the cohesive asymptote, with the following two interpolating functions adopted for values of β below and above this threshold (Fig. 7):

$$\Delta = \left(\frac{1}{\tan\beta} + \mathrm{A}\, M^{\mathrm{B}}\right) e^{-\mathrm{C}\, M} \text{ for } \beta \le 53° \tag{12a}$$

$$\Delta = \left(\frac{1}{\tan\beta} + \frac{M}{\mathrm{A} + \mathrm{B}\, M}\right) e^{-\mathrm{C}\, M} \text{ for } \beta > 53° \tag{12b}$$

where A, B and C are fitting parameters, whose values are given in Table 1. In both Eqs. (12a) and (12b), the frictional contribution Δ correctly equals $\frac{1}{\tan\beta}$ when $M = 0$ while it vanishes when $M = \infty$ due to the negative exponential factor. The use of two distinct mathematical interpolations for different inclination ranges, as in Eqs. (12a) and (12b), introduces a slight discontinuity in the computed values of the normalised factor of safety F at $\beta = 53°$. Although this discontinuity is only marginal, future research will develop a unified interpolation across the entire slope inclination range.

To facilitate application of the proposed formulation, the values of the asymptotic slope N_c and fitting parameters A, B and C have been further interpolated across slope inclinations β using linear expressions, which are reported in Table 2 and illustrated graphically in Fig. 5.

The above modelling choice is validated in Fig. 8, which assesses the interpolation of the normalised factor of safety F by Eqs. (10) and (12) using the parameter values in Table 2. Inspection of Fig. 8 indicates an excellent match between computed data and interpolating curves, up to very large values of the material parameter M, for all inclinations β (including $\beta = 50°$, which falls within the transition range). Consistent with the values of N_c in Fig. 5a, Fig. 8 shows that the linear asymptote is fixed for $\beta \le 53°$, whereas it varies with the slope inclination for

Table 2
Parametric functions for the dimensionless relationship between normalised factor of safety F and material parameter M.

Parameter	Inclination $\beta \le 53°$	Inclination $\beta > 53°$
N_c	5.52	$7.85–0.044\beta$
A	$4.78–0.069\beta$	0.079
B	0.404	$0.707 + 0.003\beta$
C	$2{\cdot}10^{-8}$	$1{\cdot}10^{-8}$

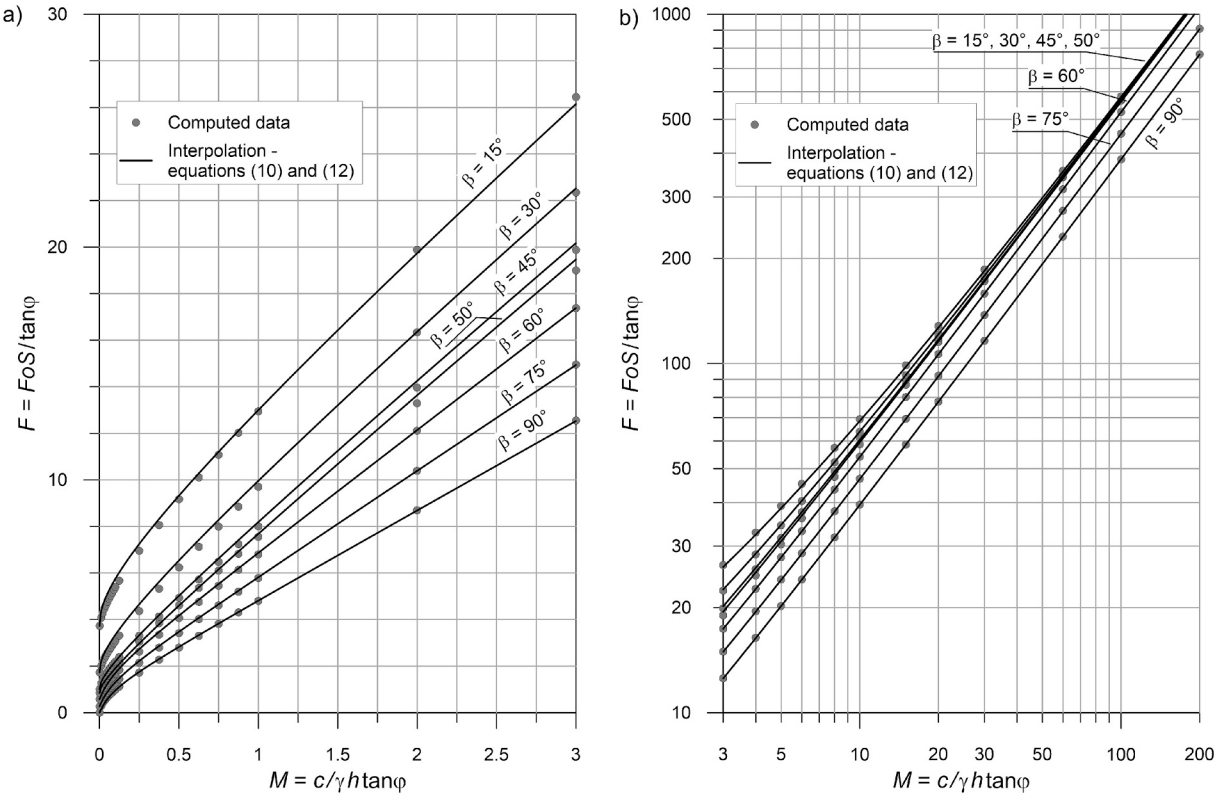

Fig. 8. Dimensionless chart relating the normalised factor of safety F to the material parameter M for different inclinations β: a) $0 \leq M \leq 3$ and b) $3 \leq M \leq 200$.

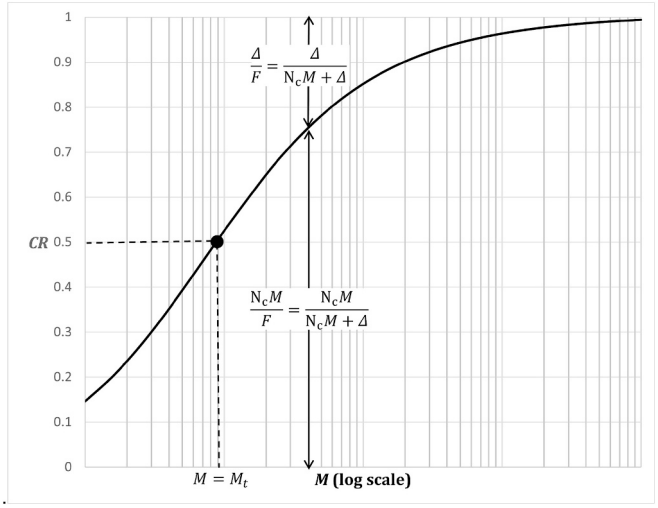

Fig. 9. Schematic variation of cohesive ratio CR with the material parameter M for a generic inclination β.

$\beta > 53°$.

The interpolation of Fig. 8 achieves a correlation coefficient $R^2 > 0.9999$, thereby ensuring an accurate and numerically stable evaluation of the factor of safety without the need of stability analyses. It is important to note that the proposed equations are only as accurate as the underlying calibration data and are therefore strictly valid over that range. Within these limits, the proposed interpolation demonstrates good agreement with that of Carranza-Torres and Hormazabal (2018), which similarly calculates the factor of safety as a function of the material parameter, albeit without explicitly distinguishing between cohesive and frictional components. Notably, the proposed interpolation covers a broad spectrum of material parameters and slope inclinations, including vertical cuts, thus ensuring general applicability.

Table 3
Threshold values of the material parameter M_t for different inclinations β.

Slope inclination, β [°]	Threshold material parameter, M_t
15	1.490
20	1.166
25	0.937
30	0.760
35	0.615
40	0.493
45	0.388
50	0.298
55	0.273
60	0.256
65	0.240
70	0.224
75	0.208
80	0.190
85	0.170
90	0.145

As discussed in previous works (e.g., Carranza-Torres and Hormazabal, 2018; Huang and Ji, 2022; Huang, 2023; Sampa and Schorr, 2024), such closed-form formulations are particularly advantageous for computationally demanding applications requiring numerous slope stability evaluations across diverse material and geometric configurations. For instance, this applies to landslide susceptibility mapping (Rahardjo et al., 2023) and large-scale statistical uncertainty analyses.

The cohesive ratio CR is here defined as the fraction of the normalised factor of safety F attributable to cohesive strength according to Eqs. (10) and (12). It can be computed for each value of the material parameter$M$ and slope inclination β as:

$$CR = \frac{N_c M}{F} = \frac{N_c M}{N_c M + \Delta} \tag{13}$$

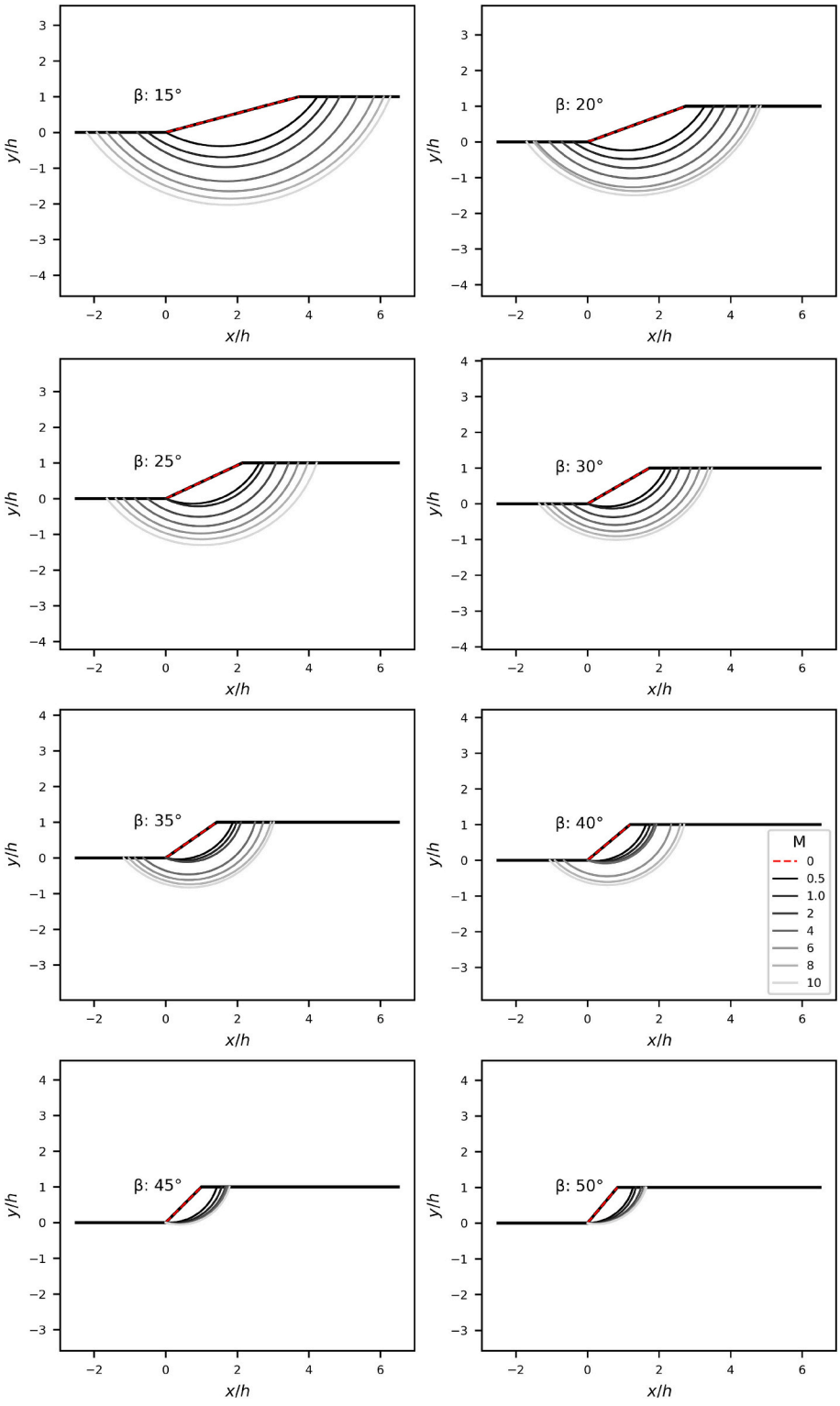

Fig. 10. Variation of normalised critical slip geometry with the material parameter M for different inclinations β.

As schematically shown in Fig. 9, the cohesive ratio CR approaches zero at low values of M, where friction dominates, while it tends to one at high values of M, where cohesion dominates. For each slope inclination β, a threshold value of the cohesive ratio $CR = 0.5$ can be defined, along with the corresponding threshold value of the material parameter M_t, marking the transition from predominantly frictional to predominantly cohesive behaviour (Fig. 9). Specifically, when $M < M_t$, the frictional contribution to the normalised factor of safety exceeds the cohesive one, whereas the opposite holds when $M > M_t$.

Table 3 presents the threshold values of the material parameter M_t computed by Eqs. (10) and (12), using the parameter values in Table 2, for different slope inclinations β.

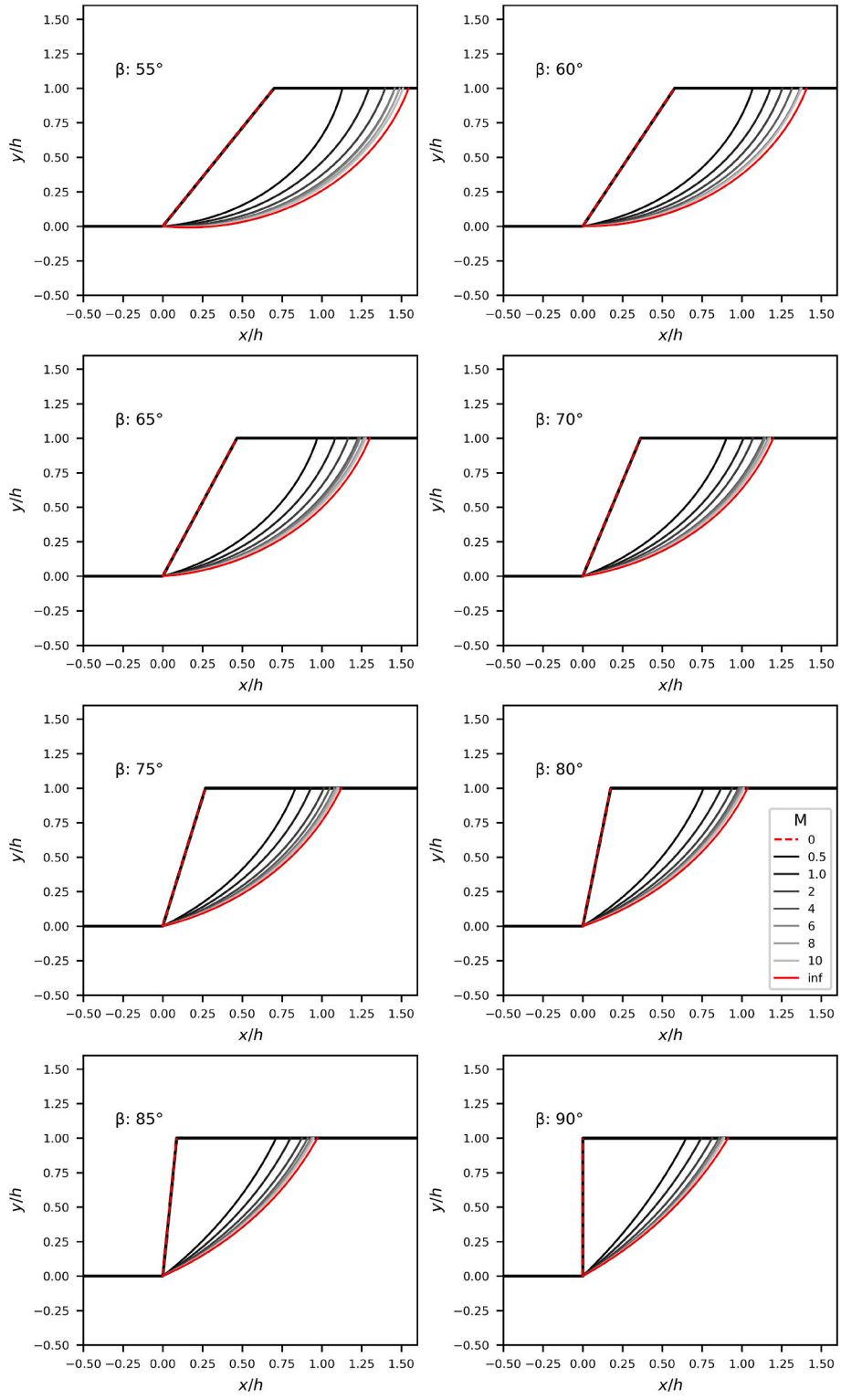

Fig. 10. (*continued*).

5. Geometry of normalised critical slip surfaces as a function of dimensionless variables M and β

Fig. 10 plots the normalised critical slip surfaces for selected ranges of the material parameter $M \leq 10$ and inclination $15^\circ \leq \beta \leq 90^\circ$ in the non-dimensional plane $\left(X = \frac{x}{h}, Y = \frac{y}{h}\right)$. For completeness, the normalised critical slip surfaces of a purely cohesive slope ($M = \infty$) are also included, but only for $\beta \geq 55^\circ$, since for shallower inclinations they become infinitely deep and cannot be represented graphically (Fellenius, 1936; Taylor, 1937; Baker, 2003). To enhance readability, different geometrical scales have also been adopted for slope inclinations $\beta \leq 50^\circ$ and $\beta \geq 55^\circ$, respectively.

For all inclinations, the critical slip line coincides with the slope surface when $M = 0$ (i.e. purely frictional material) and progressively deepens as M grows (i.e. increasingly cohesive material). Additionally,

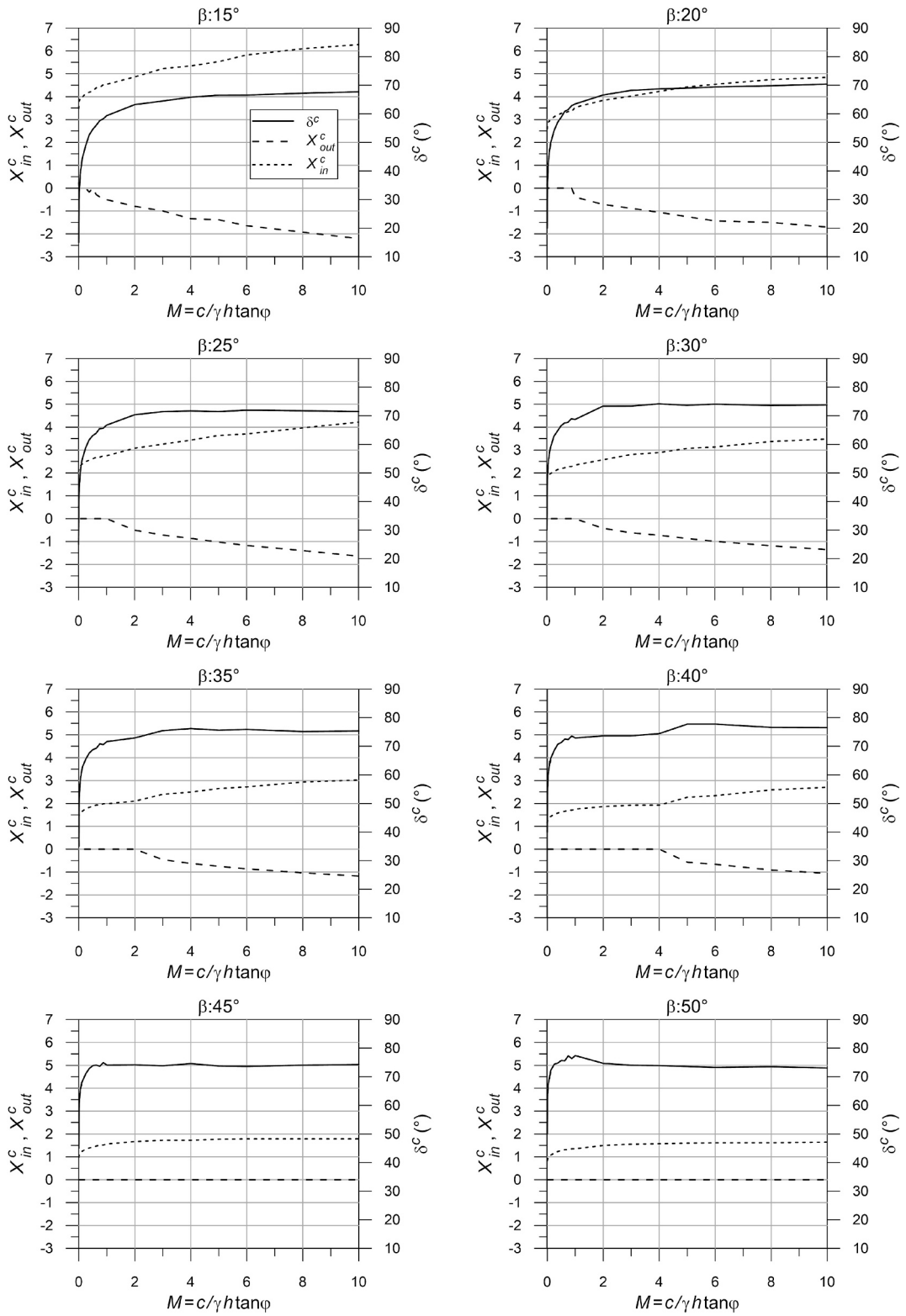

Fig. 11. Dimensionless chart relating the critical slip parameters X^c_{in}, X^c_{out} and δ^c to the material parameter M for different inclinations β.

the horizontal extent of the critical slip surface decreases with increasing slope steepness β. Specifically, for $\beta \leq 40°$, the critical slip surface extends well beyond both the slope toe and crest, reaching distances that exceed twice the slope height at higher values of M. In contrast, for $\beta \geq 45°$, the slip surface consistently emerges at the slope toe and extends no more than one times the slope height beyond the crest for all considered values of M. Finally, the critical slip surface exhibits progressively lower curvature as the slope becomes steeper, approaching a nearly linear geometry at $\beta = 90°$.

The minimisation of Eq. (2) enables the construction of non-dimensional charts enabling a rapid determination of the critical slip geometry in terms of the newly proposed parameter triplet for selected

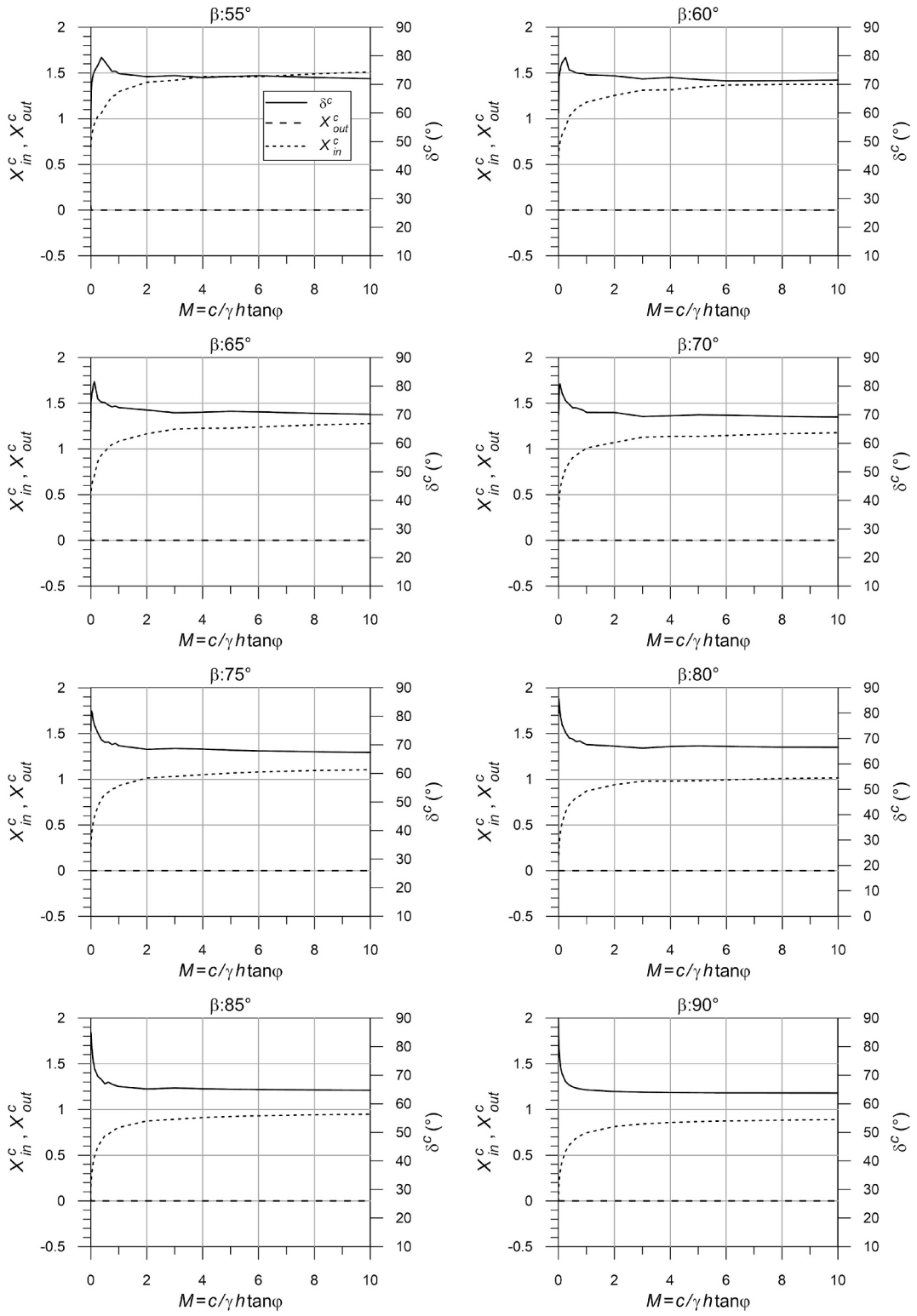

Fig. 11. (*continued*).

pairs of M and β values. Specifically, Fig. 11 illustrates the variation of the critical triplet $X^c_{in} = \frac{x^c_{in}}{h}$, $X^c_{out} = \frac{x^c_{out}}{h}$ and δ^c across selected ranges of the material parameter $M \leq 10$ and inclination $15° \leq \beta \leq 90°$, covering the same slope properties and geometry of Fig. 10.

As already qualitatively observed in Fig. 10, Fig. 11 indicates that, for $\beta \geq 45°$, the exit abscissa X^c_{out} is always zero meaning that all slip lines exit at the slope toe for the chosen range of M. Conversely, for $\beta \leq 40°$, the exit abscissa X^c_{out} exhibits a discontinuity, indicating a transition of the exit point from the slope toe to the lower horizontal ground, at a value of M which increase with growing slope inclination. These transition values of M differ from the threshold values M_t in Table 3, which instead decrease with growing slope inclination. The shift from superficial to deep failure mechanisms therefore occurs at a value of cohesive ratio CR that increases with growing slope inclination.

Finally, consistent with Fig. 10, Fig. 11 indicates that the difference between the entry and exit abscissae X_{in}^{c} and X_{out}^{c} decreases as β increases, confirming a reduction in the horizontal extent of the critical slip mechanism with growing slope inclination.

6. Conclusions

This paper provides insights into the dimensionless stability analysis of homogeneous slopes by incorporating a novel, physically based non-dimensional parametrisation of the slip geometry into Bishop (1955) limit equilibrium equation. The novel parameter triplet ensures that all and only viable mechanisms are analysed, thus improving computational accuracy and efficiency. The advantage is particularly clear when analysing vertical or nearly vertical slopes, where the critical slip circle approximates a straight line. In such cases, the conventional parameterisation struggles to accurately capture the critical failure mechanism, which approaches a circle of infinite radius.

Note that the analysis presented in this work assumes circular slip surfaces, coherent with Bishop (1955) limit equilibrium equation, and does not account for the presence of tension cracks or a firm stratum at finite depth.

Drawing on prior studies by Carranza-Torres and Hormazabal (2018) and Carranza-Torres (2021), which adopted a different parameterisation of slip circles, this work employs an in-house optimisation code to minimise the non-dimensional form of Bishop (1955) equation. This minimisation has been performed for multiple combinations of slope inclination β and material parameter $M = \frac{c}{\gamma\, h \tan\varphi}$, leading to the calculation of the corresponding normalised factor of safety $F = \frac{FoS}{\tan\varphi}$ and critical slip circle. The computed pairs of F and M have subsequently been interpolated, for each slope inclination β, using an original physically based expression that distinctly accounts for the contributions of cohesive and frictional strength. This interpolation reveals the existence of a slope inclination marking a transition in frictional behaviour, as previously observed by Taylor (1937) for cohesive behaviour. It also naturally predicts the two limit cases of purely frictional slope with $c = 0$, resulting in $M = 0$, and purely cohesive slope with $\varphi = 0$, resulting in $M = \infty$. The proposed formulation constitutes an improvement upon existing equations, which do not explicitly distinguish between the contributions of cohesive and frictional strength to slope stability.

The proposed interpolation shows an excellent agreement with computed data, exhibiting a correlation coefficient R^2 that exceeds 0.9999. Additionally, it is highly versatile, covering the full range of inclinations, up to vertical, and a broad spectrum of material parameter values, from zero to 200, effectively accounting for all realistic combinations of cohesion, friction angle, slope height and soil unit weight. As such, it enables an accurate and direct calculation of the factor of safety for any homogeneous slope, without the need for stability analyses. This is particularly advantageous for applications requiring multiple safety evaluations across varying material and/or geometric configurations, such as landslide risk mapping or statistical uncertainty analyses. The proposed interpolation is however limited to dry homogeneous slopes, and future research will focus on incorporating the effects of pore water pressure and layered soils.

Finally, the minimisation of the non-dimensional form of Bishop (1955) solution enables the compilation of normalised charts defining the critical failure geometry in terms of the novel slip triplet for different inclinations β and material parameters M. Within the common material parameter range, i.e. $0 \leq M \leq 10$, the critical slip circles consistently emerge at the slope toe when $\beta \geq 45^{\circ}$. Conversely, for shallower slopes with $\beta \leq 40^{\circ}$, the critical slip circles emerge at the slope toe only for low material parameter values, while they progressively deepen as M increases.

The factor of safety and failure geometry calculated by the proposed interpolation show good agreement with previous studies (Carranza-Torres and Hormazabal, 2018; Carranza-Torres, 2021), which developed similar non-dimensional tools without, however, explicitly distinguishing between the contributions of cohesive and frictional strength.

CRediT authorship contribution statement

Domenico Gallipoli: Writing – review & editing, Writing – original draft, Validation, Supervision, Project administration, Methodology, Investigation, Funding acquisition, Formal analysis, Conceptualization. **Leonardo Maria Lalicata:** Writing – review & editing, Writing – original draft, Visualization, Validation, Methodology, Investigation, Formal analysis, Data curation.

Declaration of competing interest

The authors declare that they have no known competing financial interests or personal relationships that could have appeared to influence the work reported in this paper.

Acknowledgments

The contribution from the European Union – NextGenerationEU and by the Ministry of University and Research (MUR), National Recovery and Resilience Plan (NRRP), Mission 4, Component 2, Investment 1.5, project “RAISE - Robotics and AI for Socio-economic Empowerment” (ECS00000035) through funding of the first author in the framework of the RAISE Innovation Ecosystem is gratefully acknowledged. The authors thankfully acknowledge the contributions of three anonymous reviewers and the associated editor in improving the content of the manuscript.

Appendix A

To normalise Eq. (1), all slice-dependent terms, i.e. h_i, $\sin\alpha_i$ and $\cos\alpha_i$, are first recast as functions of the slice mid-width abscissa, x_i. Fig. 1 shows that, for a circular slip surface of radius r with centre coordinates x_c and y_c, the height h_i of the *ith* slice is a function of the mid-width abscissa, x_i as:

$$\begin{cases} h_i = r\cos\alpha_i - y_c & \text{if} \quad x_i \leq 0 \\ h_i = r\cos\alpha_i - y_c + x_i\tan\beta & \text{if} \quad 0 \leq x_i \leq l \\ h_i = r\cos\alpha_i - y_c + h & \text{if} \quad x_i \geq l \end{cases} \tag{A1}$$

where β, h and l are respectively the inclination, height and length of the slope.

The sine and cosine of the angle at the base of the *ith* slice, i.e. $\sin\alpha_i$ and $\cos\alpha_i$, can also be expressed as functions of the mid-width abscissa, x_i (Fig. 1) as:

$$\sin\alpha_i = \frac{x_i - x_c}{r}$$

$$\cos\alpha_i = \sqrt{1 - \left(\frac{x_i - x_c}{r}\right)^2} \tag{A2}$$

Substitution of Eqs. (A1) and (A2) into Eq. (1) yields the following expression of the factor of safety where each summation term only depends on the slice mid-width abscissae x_i:

$$FoS = \frac{r^2}{\sum_{i=1}^{n}\gamma\left(\sqrt{r^2-(x_i-x_c)^2}-y_c+k_i\right)(x_i-x_c)}\sum_{i=1}^{n}\frac{c+\gamma\left(\sqrt{r^2-(x_i-x_c)^2}-y_c+k_i\right)\tan\varphi}{\sqrt{r^2-(x_i-x_c)^2}+\frac{(x_i-x_c)\tan\varphi}{FoS}} \tag{A3}$$

where:

$$\begin{cases} k_i = 0 & \text{if} \quad x_i \le 0 \\ k_i = x_i\tan\beta & \text{if} \quad 0 \le x_i \le l \\ k_i = h & \text{if} \quad x_i \ge l \end{cases}$$

Eq. (A3) can now be recast in a dimensionless form after scaling all geometrical variables by the slope height h, i.e. $X_i = \frac{x_i}{h}$, $X_c = \frac{x_c}{h}$, $Y_c = \frac{y_c}{h}$ and $R = \frac{r}{h}$ (Fig. 2), as:

$$F = \frac{R^2}{\sum_{i=1}^{n}\left(\sqrt{R^2-(X_i-X_c)^2}-Y_c+K_i\right)(X_i-X_c)}\sum_{i=1}^{n}\frac{M+\left(\sqrt{R^2-(X_i-X_c)^2}-Y_c+K_i\right)}{\sqrt{R^2-(X_i-X_c)^2}+\frac{X_i-X_c}{F}} \tag{A4}$$

where:

$$\begin{cases} K_i = 0 & \text{if} \quad X_i \le 0 \\ K_i = X_i\tan\beta & \text{if} \quad 0 \le X_i \le \dfrac{1}{\tan\beta} \\ K_i = 1 & \text{if} \quad X_i \ge \dfrac{1}{\tan\beta} \end{cases}$$

Appendix B

For case b), the lower bound δ^{min} is calculated from the trigonometric formula of the chord length applied to the two circular segments indicated in Fig. B1, which results in the following two equalities:

$$\sqrt{(X_{in}-X_{out})^2+Y_{in}{}^2} = 2R\sin\left(\delta^{min}-\gamma\right) \Longrightarrow \sqrt{(X_{in}-X_{out})^2+Y_{in}{}^2} = 2R\left(\sin\delta^{min}\cos\gamma-\cos\delta^{min}\sin\gamma\right)$$

$$\sqrt{X_{in}{}^2+Y_{in}{}^2} = 2R\sin\left(\delta^{min}-\varepsilon\right) \Longrightarrow \sqrt{X_{in}{}^2+Y_{in}{}^2} = 2R\left(\sin\delta^{min}\cos\varepsilon-\cos\delta^{min}\sin\varepsilon\right) \tag{B1}$$

where γ and ε are the angles of the chords of the two circular segments.

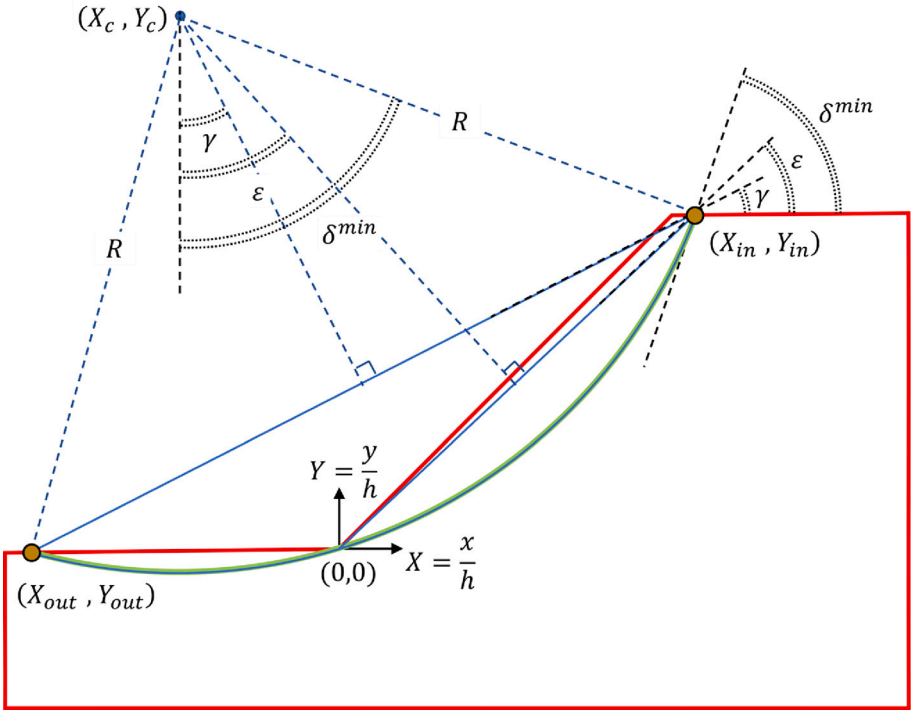

Fig. B1. Calculation of δ^{min} for case b).

Making the ratio between the two expressions of Eq. (B1) and noting that, by definition, $\cos\gamma = (X_{in}-X_{out})/\sqrt{(X_{in}-X_{out})^2+Y_{in}^2}$, $\sin\gamma = Y_{in}/\sqrt{(X_{in}-X_{out})^2+Y_{in}^2}$, $\cos\varepsilon = X_{in}/\sqrt{X_{in}^2+Y_{in}^2}$ and $\sin\varepsilon = Y_{in}/\sqrt{X_{in}^2+Y_{in}^2}$, the following equality is obtained:

$$\frac{(X_{in}-X_{out})^2+Y_{in}^2}{X_{in}^2+Y_{in}^2} = \frac{\tan\delta^{min}(X_{in}-X_{out})-Y_{in}}{\tan\delta^{min}X_{in}-Y_{in}} \tag{B2}$$

from which the value of $\tan\delta^{min}$ is calculated as:

$$\tan\delta^{min} = \frac{(2X_{in}-X_{out})Y_{in}}{X_{in}^2-X_{in}X_{out}-Y_{in}^2} \tag{B3}$$

Finally, noting from Fig. 3b that $Y_{in}=1$, the angle δ^{min} is calculated from Eq. (B3) as:

$$\tan\delta^{min} = \frac{2X_{in}-X_{out}}{X_{in}^2-X_{in}X_{out}-1} \quad \Longrightarrow \quad \delta^{min} = \arctan\frac{2X_{in}-X_{out}}{X_{in}^2-X_{in}X_{out}-1} \tag{B4}$$

For case d), the lower bound δ^{min} is calculated in a similar way as in case b). However, unlike case b), the lower bound δ^{min} is now obtained from Eq. (B3), after noting from Fig. 3d that $Y_{in}=X_{in}\tan\beta$, as:

$$\tan\delta^{min} = \frac{(2X_{in}-X_{out})\tan\beta}{X_{in}(1-\tan^2\beta)-X_{out}} \quad \Longrightarrow \quad \delta^{min} = \arctan\frac{(2X_{in}-X_{out})\tan\beta}{X_{in}(1-\tan^2\beta)-X_{out}} \tag{B5}$$

Appendix C

The mapping relationships between the proposed non-dimensional parameter triplet, i.e. X_{in}, X_{out} and δ, and the conventional one, i.e. X_c, Y_c and R, are obtained from the formula of the cord length using simple trigonometric relationships with reference to Fig. C1 as:

$$R = \frac{1}{2}\frac{\sqrt{(X_{in}-X_{out})^2+(Y_{in}-Y_{out})^2}}{\sin(\delta-\gamma)} = \frac{1}{2}\frac{\sqrt{(X_{in}-X_{out})^2+(Y_{in}-Y_{out})^2}}{\sin\delta\cos\gamma-\cos\delta\sin\gamma}$$

$$X_c = X_{in}-R\sin\delta$$

$$Y_c = Y_{in}+R\cos\delta \tag{C1}$$

The terms $\cos\gamma$ and $\sin\gamma$ in the first of the three mapping relationships of Eq. (C1) can be recast as functions of X_{in} and X_{out}, i.e.$\cos\gamma = (X_{in}-X_{out})/\sqrt{(X_{in}-X_{out})^2+(Y_{in}-Y_{out})^2}$ and

$\sin\gamma = (Y_{in} - Y_{out})/\sqrt{(X_{in} - X_{out})^2 + (Y_{in} - Y_{out})^2}$, which yields:

$$R = \frac{1}{2}\frac{(X_{in} - X_{out})^2 + (Y_{in} - Y_{out})^2}{\sin\delta(X_{in} - X_{out}) - \cos\delta(Y_{in} - Y_{out})}$$

$$X_c = X_{in} - R\sin\delta$$

$$Y_c = Y_{in} + R\cos\delta \quad \text{(C2)}$$

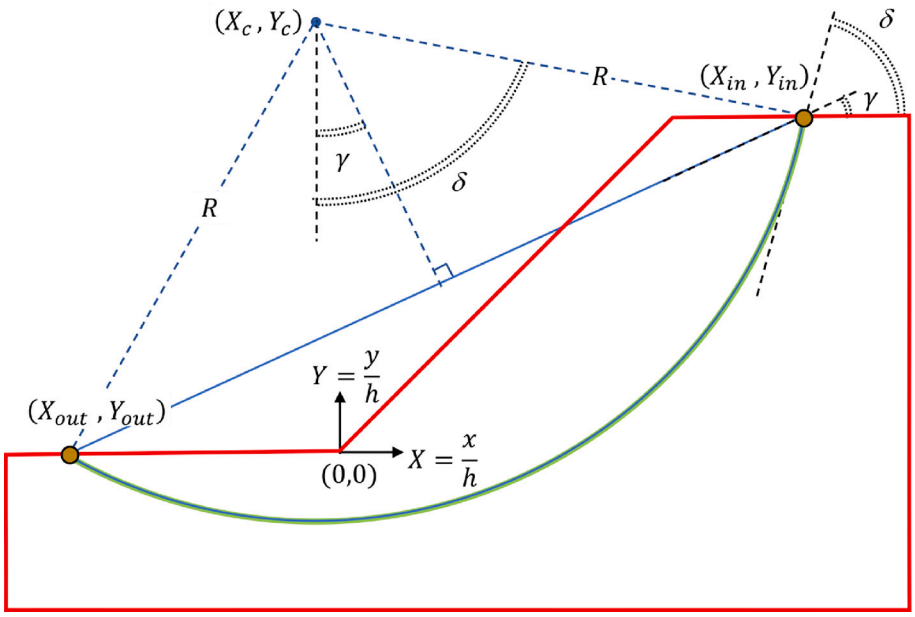

Fig. C1. Mapping relationship between the normalised parameter spaces (X_c, Y_c, R) and $(X_{in}, X_{out}, \delta)$.

Data availability

No data was used for the research described in the article.

References

Abramson, L.W., Lee, T.S., Sharma, S.M., Boyce, G., 2002. Slope Stability and Stabilization Methods, 2nd ed. John Wiley & Sons, New York.

Baker, R., 2003. A second look at Taylor's stability chart. J. Geotech. Geoenviron. Eng. 129 (12), 1102–1108. https://doi.org/10.1061/(ASCE)1090-0241(2003)129:12(1102).

Baker, R., Shukha, R., Operstein, V., Frydman, S., 2006. Stability charts for pseudo-static slope stability analysis. Soil Dyn. Earthq. Eng. 26 (9), 813–823. https://doi.org/10.1016/j.soildyn.2006.01.023.

Barnes, G.E., 1991. A simplified version of the Bishop and Morgenstern slope-stability charts. Can. Geotech. J. 28 (4), 630–637. https://doi.org/10.1139/t91-076.

Bell, J.M., 1966. Dimensionless parameters for homogeneous earth slopes. J. Soil Mech. Found. Div. 92 (5), 51–65.

Bishop, A.W., 1955. The use of the slip circle in the stability analysis of slopes. Géotechnique 5 (1), 7–17. https://doi.org/10.1680/geot.1955.5.1.7.

Bond, A.J., Schuppener, B., Scarpelli, G., Orr, T.L.L., 2013. Eurocode 7 geotechnical design: Worked examples. In: Dimova, S., Pinto, A., Nikolova, B. (Eds.), Joint Research Centre, Institute for the Protection and Security of the Citizen. Publications Office. https://doi.org/10.2788/3398.

Carranza-Torres, C., 2021. "Computational tools for the analysis of circular failure of rock slopes". Keynote Lecture. In: Proceedings of EUROCK 2021. Mechanics and Rock Engineering from theory to practice. Turin, Italy, September 21–24, 2021.

Carranza-Torres, C., Hormazabal, E., 2018. Computational tools for the determination of factor of safety and location of the critical failure surface for slopes in Mohr-Coulomb dry ground. In: Proceedings of the International Symposium Slope Stability. Sevilla, Spain, April 11-13, 2018.

Chandler, R.J., Peiris, T.A., 1989. Further extensions to the Bishop & Morgenstern slope stability charts. Ground Eng. 22 (4). https://trid.trb.org/View/313775.

Cui, H., Ji, J., Song, J., Huang, W., 2022. Limit state line-based seismic stability charts for homogeneous earth slopes. Comput. Geotech. 146, 104749. https://doi.org/10.1016/j.compgeo.2022.104749.

Duncan, J.M., 1996. State of the art: limit equilibrium and finite-element analysis of slopes. J. Geotech. Eng. 122 (7), 577–596. https://doi.org/10.1061/(ASCE)0733-9410(1996)122:7(577).

EN 1997–1, 2004. Eurocode 7: Geotechnical design - Part 1: General rules. The European Union per regulation 305/2011, Directive 98/34/EC, Directive 2004/18/EC.

Fellenius, W., 1936. Calculation of the stability of earth dams. In: Proc. of the Second Congress of Large Dams, Washington, DC, 4, pp. 445–463.

Hoek, E., Bray, J., 1974. Rock Slope Engineering. IMM, London.

Huang, W., 2023. Stability of homogeneous slopes: from chart to closed-form solutions and from deterministic to probabilistic analysis. Int. J. Geomech. 23 (9), 04023136.

Huang, W., Ji, J., 2022. Closed-form solutions for regional earthquake–induced landslide prediction: Rotational failure mechanism. Landslides 19 (11), 2671–2684. https://doi.org/10.1007/s10346-022-01916-5.

Lalicata, L.M., Bressan, A., Pittaluga, S., Tamellini, L., Gallipoli, D., 2024. An efficient slope stability algorithm with physically consistent parametrisation of slip surfaces. Int. J. Civ. Eng. 23, 671–682. https://doi.org/10.1007/s40999-024-01053-1.

Leshchinsky, D., San, K.C., 1994. Pseudostatic seismic stability of slopes: design charts. J. Geotech. Eng. 120 (9), 1514–1532.

Li, C., Su, L., Liao, H., Zhang, C., Xiao, S., 2021. Modeling of rapid evaluation for seismic stability of soil slope by finite element limit analysis. Comput. Geotech. 133, 104074. https://doi.org/10.1016/j.compgeo.2021.104074.

Michalowski, R.L., 1995. Slope stability analysis: a kinematical approach. Geotechnique 45 (2), 283–293.

Michalowski, R.L., 2002. Stability charts for uniform slopes. J. Geotech. Geoenviron. Eng. 128 (4), 351–355. https://doi.org/10.1061/(ASCE)1090-0241(2002)128:4(351).

Morgenstern, N.R., Price, V.E., 1965. The analysis of the stability of general slip surfaces. Géotechnique 15 (1), 79–93. https://doi.org/10.1680/geot.1965.15.1.79.

O'Connor, M.J., Mitchell, R.J., 1977. An extension of the Bishop and Morgenstern slope stability charts. Can. Geotech. J. 14 (1), 144–151. https://doi.org/10.1139/t77-011.

Park, D., 2025. Stability analysis of earth slopes with counterweight fill: Kinematic limit analysis. Eng. Geol. 351, 108027. https://doi.org/10.1016/j.enggeo.2025.108027.

Rahardjo, H., Zhai, Q., Satyanaga, A., Li, Y., Rangarajan, S., Rahimi, A., 2023. Slope susceptibility map for preventive measures against rainfall-induced slope failure. Urban Lifeline 1 (5). https://doi.org/10.1007/s44285-023-00006-9.

Read, J., Stacey, P., 2009. Guidelines for open pit slope design. CSIRO Publishing, Collingwood, Australia.

Sampa, N.C., Schorr, J., 2024. A novel stability equation for the estimation of the factor of safety for homogeneous dry finite slopes. Int. J. Numer. Anal. Methods Geomech. 48 (9), 2430–2449. https://doi.org/10.1002/nag.3744.

Spencer, E., 1967. A method of analysis of the stability of embankments assuming parallel inter-slice forces. Géotechnique 17 (1), 11–26. https://doi.org/10.1680/geot.1967.17.1.11.

Steward, T., Sivakugan, N., Shukla, S.K., Das, B.M., 2011. Taylor's slope stability charts revisited. Int. J. Geomech. 11 (4), 348–352. https://doi.org/10.1061/(ASCE)GM.1943-5622.0000093.

Sun, J., Zhao, Z., 2013. Stability charts for homogenous soil slopes. J. Geotech. Geoenviron. Eng. 139 (12), 2212–2218. https://doi.org/10.1061/(ASCE)GT.1943-5606.0000938.

Taylor, D.W., 1937. Stability of earth slopes. J. Boston Soc. Civ. Eng. XXIV (3), 337–386.

Taylor, D.W., 1948. Fundamentals of Soil Mechanics, vol. 66, No. 2. LWW, p. 161.

Utili, S., Crosta, G.B., 2015. Analysis tools for mass movement assessment. Landslides hazards, risks and disasters, Chapter 13, 441-465. In: Shroder, John F., Davies, Tim (Eds.), Hazards and Disasters Series. https://doi.org/10.1016/B978-0-12-396452-6.00013-6.

Vo, T., Russell, A.R., 2017. Stability charts for curvilinear slopes in unsaturated soils. Soils Found. 57 (4), 543–556. https://doi.org/10.1016/j.sandf.2017.06.005.

Wyllie, D.C., Mah, C., 2004. Rock Slope Engineering. CRC Press.